Article:

Zhang, C., Nadimi, S., Maramizonouz, S. et al. (2 more authors) (2024) A discrete element model of high-pressure torsion test to assess the effect of particle characteristics in the interface. Journal of Tribology, 146 (8). 081501. ISSN 0742-4787

https://doi.org/10.1115/1.4065230

A discrete element model of high-pressure torsion test to assess the effect of particle characteristics in the interface

Chao Zhang, first author
School of Engineering, Newcastle University,
Newcastle upon Tyne, NE1 7RU, UK
e-mail: c.zhang54@newcastle.ac.uk

Sadegh Nadimi[1], second author
School of Engineering, Newcastle University,
Newcastle upon Tyne, NE1 7RU, UK
e-mail: sadegh.nadimi-shahraki@newcastle.ac.uk

Sadaf Maramizonouz, third author
School of Engineering, Newcastle University,
Newcastle upon Tyne, NE1 7RU, UK
e-mail: sadaf.maramizonouz@newcastle.ac.uk

David Milledge, fourth author
School of Engineering, Newcastle University,
Newcastle upon Tyne, NE1 7RU, UK
e-mail: david.milledge@newcastle.ac.uk

Roger Lewis, fifth author
Leonardo Centre for Tribology, Department of Mechanical Engineering, University of Sheffield
Sheffield, S1 3JD, UK
e-mail: roger.lewis@sheffield.ac.uk

[1] Corresponding author

Abstract

Sand particles have been used since the early stages of the railway industry to increase adhesion at the wheel-rail contact. However, there is a limited understanding of how sand particle characteristics affect the tribological performance of the wheel-rail contact. In this work, the high-pressure torsion test used as a small-scale simulation of the interface is numerically modelled using the discrete element method (DEM). The DEM model is then utilised to investigate the effect of different particle characteristics on the frictional performance of wheel-rail contact which can provide more insight on micromechanical observations. The effects of various particle characteristics including their size, their number, the number of fragments the particles break into, and the parameters defining the behaviour of the bonds between particle fragments on the coefficient of traction (CoT) are systematically investigated. Results show that, in dry contacts, the coefficient of traction decreases when the size or number of sand particles increase. This can be attributed to the formation of weak shear bands between the fragments. Further investigation is needed for wet and leaf-contaminated contacts. It is also found that the CoT is more sensitive to the stiffness of the bond between the fragments of a broken particle compared to the strength of the bond. A limiting value for bond strength was identified, beyond which the sand particles exhibited ductile behaviour rather than the expected brittle fracture. The findings from this study can be useful for future research on adhesion management in wheel-rail contact.

Keywords: High-pressure torsion; Discrete element method; Sanding; Particle characteristics; Coefficient of traction

1. Introduction

It is estimated that each year, the UK rail industry spends around £350 million to manage low adhesion[2], which is a risk to the safety of the rail transport operation [1] and can result in accidents due to delayed braking, passing signals at danger, or even collisions [2]. In addition, low wheel-rail adhesion can prevent trains from accelerating effectively, leading to timetable delays and thus rising costs [1,3]. One of the main causes of low adhesion is the presence of a third-body layer (i.e., contaminants) such as oil [4], water [5,6], oxides [5], and leaf layers [7] bonded to the railhead at the wheel-rail contact.

One solution to increase the wheel-rail adhesion is depositing dry sand particles through a hose in a stream of compressed air from an on-board sand hopper onto the wheel-rail contact surface [8]. The presence of sand alters the characteristics of the contact area between the wheel and the rail and thus recovers adhesion. Another solution is utilising friction modifiers [3] that contain sand particles. These are prepared by mixing the sand particles in a gel medium and can be applied directly onto the railhead via a pumping system in track-side applicators, or via train-borne applicators mounted on maintenance trains.

The characteristics of the sand particles such as their size, shape, and hardness can affect the wheel-rail traction. Experimental studies performing field tests or using laboratory-based set-ups such as full-scale test rigs [9–13] and High Pressure Torsion

[2] In the railway industry "adhesion" or "adhesion coefficient" is defined as the amount of traction present when the wheel-rail contact enters partial slip. In this paper, the terms are used interchangeably.

(HPT) tests [14–16] have been employed to investigate the effects of particle characteristics on the tribological behaviour of the wheel-rail contact in the presence of sand particles. HPT test is an experimental approach to study the frictional properties of wheel-rail contacts with and without the presence of sand particles [14–17]. During the HPT test, two specimens, one representing the wheel and the other representing the rail, are compressed together at a given contact pressure to form an annulus contact. The specimens are then rotated a low speed to move to a set sweep length. The torque required to maintain the rotation is measured and the CoT at wheel-rail contact is calculated (see Evans et al. [14] for more information).

These previous experimental studies mainly focused on either the size [10–13] or the hardness [9] of the sand particles present in the wheel-rail contact area. These studies suggest that larger particle sizes and harder particles are more beneficial in restoring adhesion in leaf contaminated conditions. However, the efficiency of traction enhancement is reduced when particle sizes exceed an upper limit, or when particle hardness exceeds that of quartz [9,12]. Additionally, experimental studies have been performed using the HPT set-up to quantify the effect of particle characteristics on wheel/rail adhesion [17].

Although the above studies offer some insights on the effects of sand particle characteristics on wheel-rail traction enhancement, they are unable to provide a comprehensive view of the combined effects of particle characteristics on the frictional performance of sand in wheel-rail traction enhancement. One of the reasons behind this shortcoming is the complexity of the particle characteristics which makes it challenging to target a particular characteristic during experimental tests.

In this paper, the discrete element method (DEM) is used to simulate the HPT test set-up to individually investigate the effect of different particle characteristics on the coefficient of traction at wheel-rail contact. At a macroscopic level, the tribological performance of the wheel-rail contact is quantified by estimating the CoT while at the microscopic level, the effect of fragments generated by the breakage of the sand particles during the HPT test is investigated on the tribological characteristics of the wheel-rail contact. This can help in improving the current understanding of how the particles affect the tribological performance of wheel-rail contact and lead in proposing "the best candidate particle" for traction enhancement.

2. Methodology

2.1 Discrete element method

DEM is a well-established and versatile numerical technique for modelling particulate systems which was originally developed by Cundall and Strack [18]. In this study, DEM is used to model the dynamic behaviour of sand particles in the wheel-rail contact area during compaction and torsion phases of the HPT test. The sand particles are assumed to be rigid and discrete objects, and Newton's laws of motion are used to model the translational and rotational motions of each individual particle [18,19]:

$$m_i \cdot \frac{dv_i}{dt} = \sum F_{c,i} + m_i g \tag{1}$$

$$\frac{d\left(I_i \cdot \omega_i\right)}{dt} = R_i \cdot \sum M_{c,i} \tag{2}$$

where v_i, ω_i, m_i and I_i are the particle's translational velocity, angular velocity, mass, and moment of inertia, respectively. $F_{c,i}$ is the contact force in the normal and tangential directions, which results from the interaction between each particle with its neighbouring particles or wheel and rail specimens. $M_{c,i}$ is the contact torque, which is derived from the normal and tangential contact force, and R_i is the rotation matrix from the global to the local coordinate system.

In this study, the Hertz-Mindlin (no slip) contact model is employed, in which the normal and tangential force components are based on Hertz contact theory [20] and Mindlin-Deresiewicz's work [21,22]. The damping component of the forces in both normal and tangential directions and the damping coefficient are linked to the coefficient of restitution [23]. In addition, the tangential friction force follows the Coulomb's law of friction [18] and rolling friction is represented as a directional constant torque model independent of the contact [24].

The normal force $\left(f_n\right)$ and normal damping force $\left(f_n^d\right)$ are given by:

$$f_n = \frac{4}{3} E^* \sqrt{R^*} \delta_n^{\frac{3}{2}} \tag{3}$$

$$f_n^d = -2\sqrt{\frac{5}{6}} \beta \sqrt{S_n m^*} v_n^{rel} \tag{4}$$

where E^*, R^*, m^*, β, v_n^{rel}, δ_n, and S_n ($= 2E^*\sqrt{R^*\delta_n}$) are defined as the equivalent Young's modulus, the equivalent radius, the equivalent mass, the damping coefficient, the normal component of the relative velocity, the normal overlap, and the stiffness in the normal direction.

The tangential force $\left(f_t\right)$ and damping force in the tangential direction $\left(f_t^d\right)$, are given by:

$$f_t = -S_t \delta_t \tag{5}$$

$$f_t^d = -2\sqrt{\frac{5}{6}}\beta\sqrt{S_t m^*}\, v_t^{rel} \tag{6}$$

where v_t^{rel} and δ_t are defined as the relative tangential velocity and the tangential overlap. S_t ($= 8G^*\sqrt{R^*\delta_n}$) is the tangential stiffness, which depends on the equivalent shear modulus (G^*), the equivalent radius (R^*), and the normal overlap (δ_n).

Through the simulations it is assumed that particles can indent into the metal surface, but as they follow elastic contact behaviour, they will fully recover from their deformation. For simplicity, the surface damage is not considered here.

The materials used for rail specimen, wheel specimen, and rail sands are: R260 steel, R8T steel, and silica sand. Input parameters for the particles and their geometry are listed in **Table 1**.

The EDEM™ software package (version 7.1.0) developed by Altair is used to investigate the effect of sand particle characteristics on the friction at the wheel-rail contact.

2.2 Scaling of the Parameters

To ensure the stability and accuracy of the numerical computations, the simulation time step is usually selected to be equal or smaller than 20% of Rayleigh's time step, T_R [25]:

$$T_R = \frac{\pi R}{0.163\upsilon_m + 0.8766}\sqrt{\frac{\rho}{G}} \tag{7}$$

where R is the radius, ρ is the density, G is the shear modulus, and υ_m is the Poisson's ratio of the particle, respectively.

In this study, the 20% of Rayleigh's time step would be too small due to the size and stiffness of the fragments, which would increase the computational time. Therefore, following the scaling criteria proposed in [26–28] and Eq. (7), the actual Young's modulus (70 GPa) and density (2650 kg/m^3) of sand are adjusted appropriately (please refer to **Table 1** for the scaled parameters) allowing the time step to be increased from 10^{-8} to 10^{-7} s.

To test the validity of the results after scaling, HPT simulations with actual and scaled sand particles have been carried out on a core i5 Dell laptop to compare the effects of scaling on the numerical data for wheel-rail traction presented in **Fig. 1** as well as the computation time. In these simulations, the contact pressures of the actual and scaled sand particles are 1000 MPa and 10 MPa, respectively.

It can be observed from **Fig. 1** that graphs for coefficient of traction versus displacement show similar trends for the two cases and the traction value is reduced by only 0.04 when using scaled parameters. However, the average computation time for the simulation with the scaled particle characteristics is around 5 hours, while the simulation with the actual sand particle characteristics takes over a week. Therefore, the adjusted parameters for sand (i.e., **Table 1**) are used for all simulations in this study.

2.3 Bonded Particle Model

The breakage of a single sand particle into several fragments under mechanical load can be modelled in DEM under [29–31], using the bonded particle model (BPM) developed by Potyondy and Cundall [32].

In BPM, each individual particle is represented as a cluster of independent spherical fragments bonded together with a finite-sized bond which can resist tension pulling fragments apart [33]. An image of a modelled sand particle is presented in **Fig. 2** with the red parts representing the bonds between fragments.

Each bond is modelled as a set of elastic springs distributed on the circular cross-section at the surface of each of the fragments, transferring the translational and rotational motion that one fragment experiences to the other fragments to which it is bonded. In addition, this bond introduces forces that can resist normal and tangential motions, thus limiting stretching between fragments. After bonding, the forces and moments acting on the bond are adjusted incrementally at every time step which can be written as follows:

$$\delta F_n = -v_n k_n A \delta t \tag{8}$$

$$\delta F_t = -v_t k_t A \delta t \tag{9}$$

$$\delta M_n = -\omega_n k_t J \delta t \tag{10}$$

$$\delta M_t = -\omega_t k_n \frac{J}{2} \delta t \tag{11}$$

where A ($= \pi R_B^2$) is the area, J ($= \frac{1}{2}\pi R_B^4$) is the polar moment of inertia, R_B is the radius of bond, respectively. k_n and k_t are the normal and shear stiffness of bonds. v_n and v_t are the velocities of the fragments in the normal and tangential direction. ω_n and ω_t are the normal and tangential angular velocities of the fragments. In the above equations, multiplying the time step (δt) with the normal velocities (v_n) and tangential velocities (v_t) of the fragments calculates the relative displacement and shear displacement increments. Likewise, the relative rotation and tangential rotation increments can be obtained by multiplying the time step (δt) with the angular velocities of the fragments in the normal (ω_n) and tangential (ω_t) direction, which can then be used to account for stretching of the bonds in any direction.

In addition, δF_n, δF_t, δM_n, and δM_t are the incremental normal forces, incremental tangential forces, incremental normal moments, and incremental tangential moments of the bonds, which can be used to simulate the bond breakage over many time steps. The equations used to determine whether the normal and tangential stress exceeds some predefined value can be written as follows:

$$\sigma_{\max} < \frac{-F_n}{A} + \frac{2M_t}{J} R_B \tag{12}$$

$$\tau_{\max} < \frac{-F_t}{A} + \frac{M_n}{J} R_B \tag{13}$$

where $\sigma_{\max}$ and $\tau_{\max}$ are the critical normal and tangential stress cut-off values respectively.

To determine the size of the fragments, a sample of the crushed sand collected from the railhead has been analysed using laser diffraction (**Fig. 3**). For computational efficiency of the model, a constant value of 100 μm (<D_{90}) has been chosen as the diameter of the spherical fragments. Considering the brittle characteristics of sand, the bond properties such as bond stiffness, bond strength, and bonded disk scale (i.e., the ratio of the radius of a bond between fragments to the radius of the smallest fragment in a bond pair) for base case used in the HPT modelling are presented in **Table 2**.

2.4 High-Pressure Torsion model set-up

The HPT rig has been used to experimentally assess the frictional characteristics between two surfaces, in the presence of a third body layer such as sand particles (see Evans et al. [14] for more details). The geometrical set-up for the DEM model is constructed in accordance with the HPT rig used for the experiments by Evans et al. [14]. The geometry of the HPT set-up and the dimensions of the wheel-rail contact area used in the DEM model is shown in **Fig. 4**.

2.5 The effective radius of friction

In the HPT test, the effective radius of friction (ERF) is calculated using the outer and inner radius of the contact area which for the set-up used here is equal to 7.29 mm. The ERF can be more accurately estimated by considering the distance of each single particle fragment to the centre of the annular contact area. The ERF considering all the present particle fragments can be computed for each numerical simulation case by defining the average effective radius of friction (ERF_{avg}):

$$ERF_{avg} = \frac{\sum_{i} \sqrt{\left|\left(x_i - x_o\right)\right|^2 + \left|\left(z_i - z_o\right)\right|^2}}{N} \tag{14}$$

where x_i and z_i are the coordinates of each fragment on the x-z plane, x_o and z_o are the coordinates of the centre of the annular contact area on the x-z plane, and N is total number of fragments present in the contact area.

Once the ERF_{avg} is calculated, the coefficient of traction can then be estimated [15]:

$$CoT = \frac{F_S}{F_N} = \frac{T_m / ERF_{avg}}{F_N} \tag{15}$$

where F_N is the normal load, F_S is the shear force, and T_m is the torque measured by the HPT apparatus.

3. Results and discussion

First, the simulation results for the cases without and with sand particles present at the wheel-rail contact are compared to the experimental data obtained from HPT tests. Then, the effects of the properties of the bonds between particle fragments i.e., bond stiffness and strength on the breakage behaviour of the particles as well as the traction at the wheel-rail contact is studied. Finally, the effects of the size and the number of particles present at the wheel-rail contact on the traction at the wheel-rail contact is explored. For all simulations, a constant velocity of 0.05 m/s is applied to the wheel specimen in the vertical direction to bring it into contact with the rail specimen and achieve the required contact pressure of 10 MPa. The rail specimen then starts to rotate at a constant angular velocity of 1 deg/s until the end of the simulation when the sweep length reaches 0.4 mm. The details of all the case studies investigated through numerical simulations is summarised in **Table 3**.

3.1 Numerical investigation of the metal-to-metal contact

The metal-to-metal contact between the wheel and the rail specimens of the HPT set-up is simulated for two case studies of un-sanded and sanded. To represent the geometry-to-geometry interaction which is not usually accounted for in DEM modelling, steel particles with a 1 mm diameter are used to form a layer inside the rail specimen. The results of the DEM simulations are then compared to the corresponding experimental test outputs [34], as shown in **Fig. 5**. Under dry contact conditions, the HPT tests achieve a CoT of 0.74 and 0.72 in the absence and presence of sand particles, respectively. Modelling the dry metal-to-metal contact conditions in the numerical simulations results in CoT values of around 0.7 and 0.67 for the un-sanded and sanded conditions, respectively. The difference between the CoT values obtained through the experiments and the numerical simulations for the un-sanded and sanded case studies are 5.4% and 6.9%, respectively. In addition, it can be concluded that metal-to-metal contact dominates the frictional behaviour of wheel-rail contact at dry conditions, while sand-to-metal and sand-to-sand (where the contact between fragments can provide a weak shear band) contacts have little effect on the CoT, which is also in agreement with the analysis of Skipper et al. [16].

3.2 Effects of bond properties on the coefficient of traction

The effects of stiffness and the strength of the bonds between the fragments of sand particle on the CoT is investigated. The parameters used for each simulation are presented in **Table 3**.

Fig. 6, shows the effect of the different values of bond strength on the CoT while the bond stiffness remains constant. Changing the strength of the bonds between particle fragments in the range of $1e^{7}$ Pa to $1e^{10}$ Pa has a negligible effect on the COT. In addition, the number of fragments generated in the wheel-rail contact area as the particles break varies slightly for different bond strengths, while the number of fragments remains stable through the end of each simulation.

To investigate the effect of bond strength on the breakage behaviour of the sand particle during the HPT test, case study a.7 (see **Table 3**) with a particle diameter of 1.0 mm, and a bond strength and stiffness of $1.0e^{10}$ Pa and $1.0e^{10}$ N/m^3, respectively, is chosen. As shown in **Fig. 7 (a-1)**, in the first stage, when the wheel specimen is just in contact with the sand particle and before a normal load is applied to it, the particle retains its shape and remains in a steady state. In the second stage **Fig. 7 (a-2)**, as a normal load is applied to the wheel specimen, the particle is deformed by the compressive forces with a sudden increase in the compressive forces of the fragments at the centre of the particle and tensile failure at the edges of the particle. In the third stage of the compaction process **Fig. 7 (a-3)**, the particle fragments are completely detached and come into direct contact with the wheel and rail specimens, while the vertical load remains constant until the end of the test. **Fig. 7(b)** presents the difference in the angular velocity of the fragments from the beginning to the end of the torsion phase. The angular velocity of the fragments present in the central area of the fragment layer is greater than the angular velocity of the fragments presents in the surrounding area but the difference is not significantly large.

In **Fig. 7(c)**, it can be observed that the bond force increases sharply in the normal direction during the second stage of compaction while **Fig. 7(d)** shows no abrupt increase in tangential bond force. The bond force in normal and tangential directions gradually increases, but neither exceeds the corresponding critical bond strength. However, high bond strengths may lead to inappropriate breakage behaviour of the sand particles shown in **Fig. 7(e)**, where a small fraction of agglomerates accumulates at the edge of the wheel-rail intersection region at a bond strength of $1e^{10}$ Pa and the sand particles exhibit breakage behaviour of ductile material rather than the expected brittle material.

Fig. 8 presents the effect of different values of bond stiffness on the CoT while the bond strength remains constant. As the bond stiffness is changed in the range of $1e^{9}$ to $1e^{11}$, its effect on the CoT is more pronounced compared to the bond strength. Moreover, the difference in the number of fragments generated at the wheel-rail contact area due to particle breakage is minimal as the bond stiffness changes. The number of particle fragments generated for bond stiffness values below $5e^{10}$ N/m^3 remains constant until the end of the rotation. However, when the bond stiffness values surpass $5e^{10}$ N/m^3, the number of fragments generated in the contact area gradually decreases during torsion with the rate of decline even more pronounced with a higher bond stiffness (i.e., $1e^{11}$ N/m^3.

To investigate the effect of bond stiffness on the breakage behaviour of the sand particle during the HPT test, case study b.7 (see **Table 3**) with a particle diameter of 1.0 mm, and a bond strength and stiffness of $1.0e^{8}$ Pa and $1.0e^{11}$ N/m^3, respectively, is chosen. When a normal load is applied to the wheel specimen (**Fig. 9(a-1)**), the force transfers to the particles and a sudden increase in the compressive force is observed on most of the particle fragments as they extend outwards from the centre of the particle (**Fig. 9(a-2)**). The particle is completely crushed in the third stage (**Fig. 9(a-3)**) and is subjected to a continuous normal load until the end of the test. As shown in **Fig.**

9(b), there is a significant increase in the angular velocity of the fragments at the beginning of the twist and the overall angular velocity is greatest in the central region of the fragment layer. Thereafter, the angular velocity of the fragments decreases and stabilises from the middle stage of torsion to the end of the test.

In **Fig. 9(c)**, it can be seen that the normal bond strength increases sharply to about 28 N during the second stage of compaction, and exceeds the critical normal bond strength (about 67 N) at the third stage of compaction happening 1.8 s into the test. In **Fig. 9(d)**, the tangential bond force is shown to increase abruptly at the start of the twist and exceeds the critical tangential bond strength (around 385 N) at around 0.75 s into the test. When a high bond stiffness is used, the forces generated to resist bond stretching can easily exceed the critical bond strength, resulting in bond breakage and a gradual reduction in the force exerted on the bond.

3.3 Effects of particle size on the coefficient of traction

The parameters used for each simulation investigating the particle size are listed in **Table 4**, which shows that the number of particle fragments and bonds between them increase dramatically as the particle size increases. **Fig. 10** shows that the CoT decreases as the particle size increases. During the DEM modelling of the HPT tests, as the wheel specimen gradually approaches the rail specimen and compacts the particles, the sand particles with smaller sizes are completely broken. This results in the fragments becoming entirely detached from the parent particles and to come directly in contact with the wheel and rail specimens. However, as the particle diameter is increased to 2 mm, the particle will not completely break under the load resulting in the fragments clustering and forming layers at the wheel-rail contact area.

Fig. 11 presents a closer look at the force transfer mechanism. When the normal load is continuously applied to the particles with smaller sizes (**Fig. 11(a))**, the fragments are completely detached from the parent particle, forming only one layer and indenting into the surfaces of both the wheel and the rail specimens. This results in the creation of a reaction force that transmits the torsional force more effectively [5]. As shown in **Fig. 11(b)** to **11(d)**, for larger particle diameters of 1 mm, 1.5 mm, and 2 mm, the fragments break away from the parent particles during compaction, but numerous overlapping particles can be observed at the wheel-rail contact area. This indicates that some of the particle fragments have grouped into clusters, resulting in the formation of weak shear bands and lower traction forces.

Additionally, in **Fig. 11(e)**, it can be observed that for particle diameters smaller than 2 mm, the number of particle fragments in the contact remains constant during the test. However, for the particle with a diameter of 2.0 mm, as the sweep length increases, the number of fragments also increases. This is due to the expansion of the fragment layer as the wheel and rail specimens twist against each other, thus allowing more fragments to come into direct contact with the wheel and rail specimens.

The values of the peak CoT for different particle sizes obtained from the simulations are compared to the experimental data for both the dry and leaf-contaminated contact conditions provided by Skipper et al. [17] in **Fig. 12**. The simulation results show that as the particle size increases, the values of peak CoT decreases, whereas there is no clear relationship between the two in the experimental observations for each of the dry and leaf contaminated contact conditions. It is worth noting that in the DEM simulations, the particles are located at same positions used in experiments and there are no material heterogeneity effects. The peak CoT values resulting from the DEM simulations are closer to the case of a leaf-contaminated contact condition in the experiments. This may be due to the fact that the metal-to-metal contact was ignored in the DEM simulations (**Fig. 5**).

In **Fig. 13**, the branch vectors which are defined as lines connecting the centroids of each two particle fragments are presented for the four particle sizes and are coloured based on their contact normal forces. It can be observed that the branch vectors are not overlapping for the smallest sand particle with a diameter of 0.83 mm (**Fig. 13(a)**). As the size of the sand particle increases, the number of overlapping branch vectors at the central region of the particles increases sharply (**Fig. 13(b**) to **(d)**) which shows that the particles are rolling and sliding on top of each other in the central region during torsion.

3.4 Effects of number of particles on the coefficient of traction

Table 5 summarises the fragment properties and the average effective radius of friction for each simulation investigating the effects of different numbers of sand particles.

Fig. 14 shows that if 4 sand particles are present in the wheel-rail contact area, the CoT can increase up to 0.3. Increasing the number of sand particles to 8 or 16, decreases the CoT to 0.21 and 0.15, respectively. This is due to two reasons. First. increasing the number of particles increases the contact area between the fragments and the wheel and rail specimens (**Fig. 14**). Second, for higher particle number, the fragments are able to distribute more evenly over the wheel-rail contact area which can provide lubrication, consistent with the effects of the particle size.

4. Conclusions

The effects of particle characteristics on the frictional performance of the wheel-rail contact have been analysed using DEM simulations of HPT tests. The effects of metal-to-metal contact between the wheel and the rail specimens, the properties of the bonds between particle fragments after breakage (i.e., bond stiffness and strength), and the size and the number of the sand particles present at the contact on the frictional behaviour of wheel-rail contact quantified by the coefficient of traction have been investigated. It was presented that the properties of the bonds between the particle fragments affect the frictional behaviour of the wheel-rail contact to a certain extent. Compared to the bond strength, the bond stiffness has a stronger effect on the coefficient of traction. In addition, the bond properties considerably affect the breakage behaviour of the sand particles. If the bond strength exceeds beyond a limit, during compaction, the sand particles exhibit the breakage behaviour of a ductile material, rather than the expected brittle fracture. Increasing the size of sand particles was shown to decrease the coefficient of traction. As particle size increases, the number of fragments and the bonds between them increase dramatically. This hinders the fragments complete detachment from the parent particles during compaction, and results in the formation of particle fragment clusters. A high number of fragments in the contact creates weak shear bands and causing a lubrication effect. Further experimental tests are needed to confirm the conclusion of this study and refine the guidelines regarding the particle size suitable for sanding.

Acknowledgment

The authors would like to extend their gratitude to Dr William Skipper for sharing the experimental data obtained from performing the HPT tests.

Competing Interests

The authors declare that they have no known competing financial interests or personal relationships that could have appeared to influence the work reported in this paper.

Data Availability Statement

The data used to support the findings of this study are available upon request.

References

[1] Gray, P., 2018, "T1107 Sander Trials Dissemination Event," https://www.rssb.co.uk/Pages/adhesion.aspx

[2] Rail Accident Investigation Branch., 2007, "Autumn adhesion investigation Part 3: Review of adhesion-related incidents Autumn 2005," RAIB Report.

[3] Fulford, C. R., 2004, "Review of low adhesion research (T354)," RSSB Report. https://www.sparkrail.org/Lists/Records/DispForm.aspx?ID=9539./s40571-019-00288-3

[4] Beagley, T. M., McEwen, I. J., and Pritchard, C., 1975, "Wheel/Rail Adhesion—Boundary Lubrication by Oily Fluids," Wear, **31**(1), pp. 77–88.

[6] Buckley-Johnstone, L.E., Lewis, R., Six, K., Trummer, G., 2016, "Modelling and quantifying the influence of water on wheel/rail adhesion levels," RSSB Report. Available: https://www.sparkrail.org/Lists/Records/DispForm.aspx?ID=24280.

[6] Beagley, T. M., and Pritchard, C., 1975, "Wheel/Rail Adhesion — the Overriding Influence of Water," Wear, **35**(2), pp. 299–313.

[7] Ishizaka, K., Lewis, S. R., and Lewis, R., 2017, "The Low Adhesion Problem Due to Leaf Contamination in the Wheel/Rail Contact: Bonding and Low Adhesion Mechanisms," Wear, **378–379**, pp. 183–197.

[8] Rail Safety and Standards Board, 2013, "Performance and Installation Criteria for Sanding Systems (T797)," https://www.rssb.co.uk/research-catalogue/CatalogueItem/T797

[13] Zobel, F.G.R., 1974, "Development of Remedies for Poor Adhesion (IM-ADH-019)," British Rail Research. https://www.sparkrail.org/Lists/Records/DispForm.aspx? ID=9038

[10] Arias-Cuevas, O., Li, Z., Lewis, R., and Gallardo-Hernández, E. A., 2010, "Laboratory Investigation of Some Sanding Parameters to Improve the Adhesion in Leaf-Contaminated Wheel—Rail Contacts," Proceedings of the Institution of Mechanical Engineers, Part F: Journal of Rail and Rapid Transit, **224**(3), pp. 139–157.

[11] Arias-Cuevas, O., and Li, Z., 2011, "Field Investigations into the Adhesion Recovery in Leaf-Contaminated Wheel–Rail Contacts with Locomotive Sanders," P I Mech Eng F-J Rai, **225**(5), pp. 443–456.

[12] Arias-Cuevas, O., Li, Z., and Lewis, R., 2011, "A Laboratory Investigation on the Influence of the Particle Size and Slip during Sanding on the Adhesion and Wear in the Wheel–Rail Contact," Wear, **271**(1–2), pp. 14–24.

[13] Wang, W. J., Liu, T. F., Wang, H. Y., Liu, Q. Y., Zhu, M. H., and Jin, X. S., 2014, "Influence of Friction Modifiers on Improving Adhesion and Surface Damage of Wheel/Rail under Low Adhesion Conditions," Tribology International, **75**, pp. 16–23.

[14] Evans, M., Skipper, W. A., Buckley-Johnstone, L., Meierhofer, A., Six, K., and Lewis, R., 2021, "The Development of a High Pressure Torsion Test Methodology for Simulating Wheel/Rail Contacts," Tribol Int, **156**, p. 106842.

[15] Buckley-Johnstone, L. E., Trummer, G., Voltr, P., Meierhofer, A., Six, K., Fletcher, D. I., and Lewis, R., 2019, "Assessing the Impact of Small Amounts of Water and

Iron Oxides on Adhesion in the Wheel/Rail Interface Using High Pressure Torsion Testing," Tribol Int, **135**, pp. 55–64.

[16] Skipper, W. A., Nadimi, S., Chalisey, A., and Lewis, R., 2019, "Particle Characterisation of Rail Sands for Understanding Tribological Behaviour," Wear, **432–433**, p. 202960.

[17] Skipper, W. A., Nadimi, S., Watson, M., Chalisey, A., and Lewis, R., 2023, "Quantifying the Effect of Particle Characteristics on Wheel/Rail Adhesion & Damage through High Pressure Torsion Testing," Tribol Int, **179**, p. 108190.

[18] Cundall, P. A., and Strack, O. D. L., 1979, "A Discrete Numerical Model for Granular Assemblies," Géotechnique, **29**(1), pp. 47–65.

[19] Thornton, C., 2015, *Granular Dynamics, Contact Mechanics and Particle System Simulations*, Springer International Publishing, Cham.

[20] Hertz, H., 1882, "Ueber die Berührung fester elastischer Körper.," **1882**(92), pp. 156–171.

[21] Mindlin, R. D., 2021, "Compliance of Elastic Bodies in Contact," Journal of Applied Mechanics, **16**(3), pp. 259–268.

[22] Mindlin, R. D., and Deresiewicz, H., 2021, "Elastic Spheres in Contact Under Varying Oblique Forces," Journal of Applied Mechanics, **20**(3), pp. 327–344.

[23] Tsuji, Y., Tanaka, T., and Ishida, T., 1992, "Lagrangian Numerical Simulation of Plug Flow of Cohesionless Particles in a Horizontal Pipe," Powder Technology, **71**(3), pp. 239–250.

[24] Sakaguchi, H., Ozaki, E., Igarashi, T., 1993, "Plugging of the Flow of Granular Materials during the Discharge from a Silo," International Journal of Modern Physics B, **7**(09n10), pp. 1949-1963. https://doi.org/10.1142/S0217979293002705

[25] Li, Y., Xu, Y., and Thornton, C., 2005, "A Comparison of Discrete Element Simulations and Experiments for 'Sandpiles' Composed of Spherical Particles," Powder Technology, **160**(3), pp. 219–228.

[26] Behjani, M. A., Rahmanian, N., Fardina bt Abdul Ghani, N., and Hassanpour, A., 2017, "An Investigation on Process of Seeded Granulation in a Continuous Drum Granulator Using DEM," Adv Powder Technol, **28**(10), pp. 2456–2464.

[27] Hærvig, J., Kleinhans, U., Wieland, C., Spliethoff, H., Jensen, A. L., Sørensen, K., and Condra, T. J., 2017, "On the Adhesive JKR Contact and Rolling Models for Reduced Particle Stiffness Discrete Element Simulations," Powder Technol, **319**, pp. 472–482.

[28] Washino, K., Chan, E. L., and Tanaka, T., 2018, "DEM with Attraction Forces Using Reduced Particle Stiffness," Powder Technol, **325**, pp. 202–208.

[29] Wang, P., and Arson, C., 2016, "Discrete Element Modeling of Shielding and Size Effects during Single Particle Crushing," Comput Geotech, **78**, pp. 227–236.

[30] Fu, R., Hu, X., and Zhou, B., 2017, "Discrete Element Modeling of Crushable Sands Considering Realistic Particle Shape Effect," Computers and Geotechnics, **91**, pp. 179–191.

[31] Wu, M., Wang, J., and Zhao, B., 2022, "DEM Modeling of One-Dimensional Compression of Sands Incorporating Statistical Particle Fragmentation Scheme,"

Can Geotech J, **59**(1), pp. 144–157.
[32] Potyondy, D. O., and Cundall, P. A., 2004, “A Bonded-Particle Model for Rock,” Int J Rock Mech Min, **41**(8), pp. 1329–1364.
[29] Altair EDEM 2021, (n.d.). https://2021.help.altair.com/2021.1/EDEM/index.htm
[34] Skipper, W., Nadimi, S., and Lewis, R., 2021, “Sand Consist Change for Improved Track Circuit Performance (COF-UOS-03),” p. 84.

Figure Captions List

Fig. 1	Comparison of the coefficient of traction obtained from DEM modelling of the HPT set-up for the two cases using actual (red) and scaled (black) sand parameters
Fig. 2	Schematic of a sand particle represented as a cluster of spherical fragments bonded together using the bonded particle model
Fig. 3	Particle size distribution of the crushed sand obtained using laser diffraction ("% Passing" on the y-axis represents the percentage of particles in the sample that have a size smaller than or equal to a particular particle size on the x-axis)
Fig. 4	(a) The set-up used for numerical modelling of the high-pressure torsion test and (b) the dimensions of the annular contact area between the wheel and the rail specimens
Fig. 5	Comparison of the coefficient of traction obtained from DEM modelling of the HPT set-up with and without the presence of sand particles under dry contact condition with the corresponding experimental data. (The light grey particles represent the rail specimen, and the orange particles represent the fragments of sand particles)
Fig. 6	Comparison of the coefficient of traction obtained from DEM modelling of the HPT set-up using different values of bond strength (The insert graph shows the number of fragments remaining on the contact area for each value of the bond strength)
Fig. 7	The breaking behaviour of the sand particle and the evolution of the bond force in the normal and tangential directions for particle with a 1.0 mm diameter, and a bond strength and stiffness of $1.0e^{10}$ [Pa] and $1.0e^{10}$ [N/m^3], respectively, during the DEM modelling: (a) Changes in the compression force of fragments during compaction (side view), (b) Changes in the angular velocity of the fragments during torsion (top view), (c) Normal bond force, (d) Tangential bond force, and (e) the particle showing ductile behaviour when breaking

Fig. 8 Comparison of the coefficient of traction obtained from DEM modelling of the HPT set-up using different values of bond stiffness (The insert graph shows the number of fragments remaining on the contact area for each value of the bond stiffness)

Fig. 9 The breaking behaviour of the sand particle and the evolution of the bond force in the normal and tangential directions for particle with a 1.0 mm diameter, and a bond strength and stiffness of $1.0e^{8}$ [Pa] and $1.0e^{11}$ [N/m^3], respectively during the DEM modelling: (a) Changes in the compression force of fragments during compaction (side view), (b) Changes in the angular velocity of the fragments during torsion (top view), (c) Normal bond force, and (d) Tangential bond force

Fig. 10 Sand particles of different size with a diameter of: (a) 0.83mm, (b) 1.0mm, (c) 1.5mm, and (d) 2.0mm used in the DEM models and (e) comparison of the coefficient of traction obtained from DEM modelling of the HPT set-up using different particle sizes

Fig. 11 Particle breakage in the contact area, the variation in the number of fragments depending on the particle size, and the possibility of the formation of fragment clusters and weak shear bands during the DEM simulation for particles with a diameter of: (a) 0.83mm, (b) 1.0mm, (c) 1.5mm, and (d) 2.0mm, and (e) comparison of the number of fragments produced during the DEM modelling of the HPT set-up for the above four particle sizes

Fig. 12 Comparison of the peak coefficient of traction obtained from DEM modelling of the HPT set-up (blue diamond) using different particle sizes to the experimental results for dry (black square) and leaf-contaminated (green circle) contact condition by Skipper et al. 2023

Fig. 13 The contact force network formed during crushing of a particle with a diameter of: (a) 0.83mm, (b) 1.0mm, (c) 1.5mm, and (d) 2.0mm obtained from the DEM models

Fig. 14 The particle distribution used in the DEM models for different number of particles present at the wheel-rail contact area (1) before and (2) after crushing shown from the top view for: (a) 4 particles, (b) 8 particles, and (c) 16 particles and (d) comparison of the coefficient of traction obtained from DEM modelling of the HPT set-up using different number of particles at the contact area

Table Caption List

Table 1 Material properties used as input parameters in the DEM modelling of the HPT set-up

Table 2 Bond properties used as inputs in the BPM for the sand particles

Table 3 Particle properties used as input parameters in each numerical case study

Table 4 Fragment and bond properties as well as the average effective radius for each particle size

Table 5 Fragment properties and the average effective radius for the three different number of particles present on the contact area

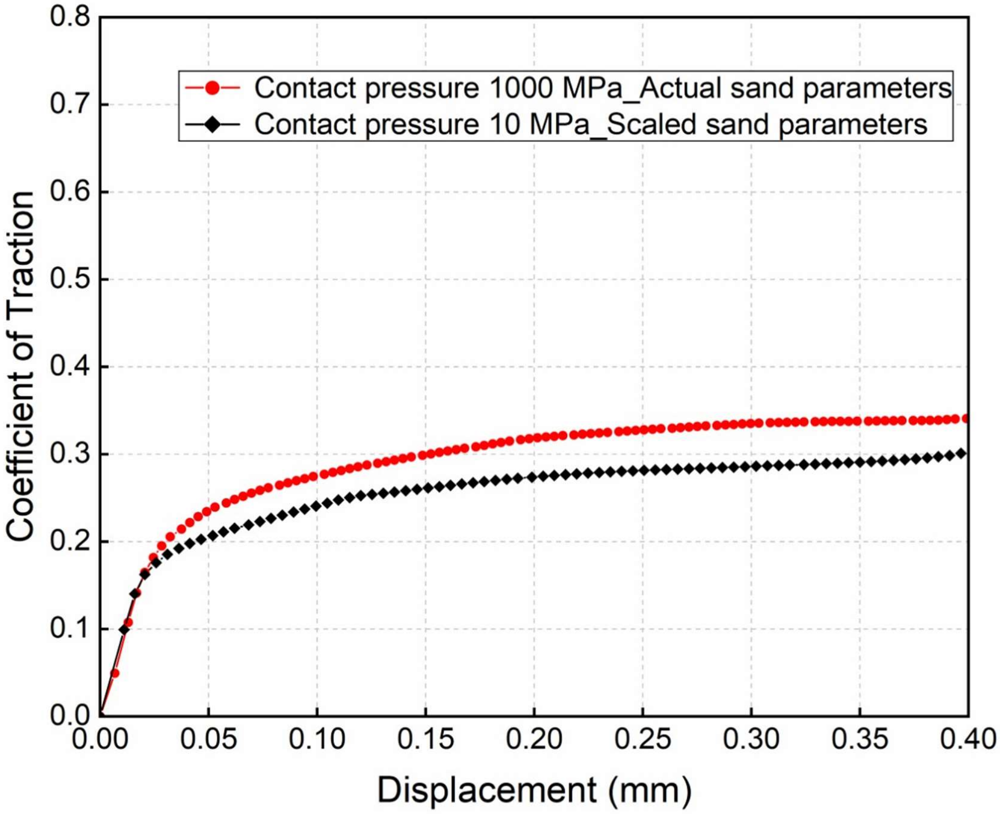

Fig. 1. Comparison of the coefficient of traction obtained from DEM modelling of the HPT set-up for the two cases using actual (red) and scaled (black) sand parameters

542

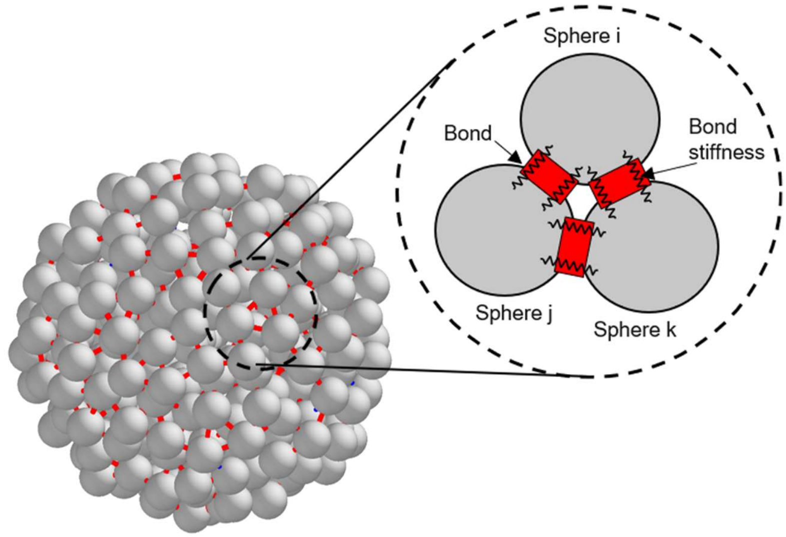

543

544 **Fig. 2.** Schematic of a sand particle represented as a cluster of spherical fragments bonded
545 together using the bonded particle model

546

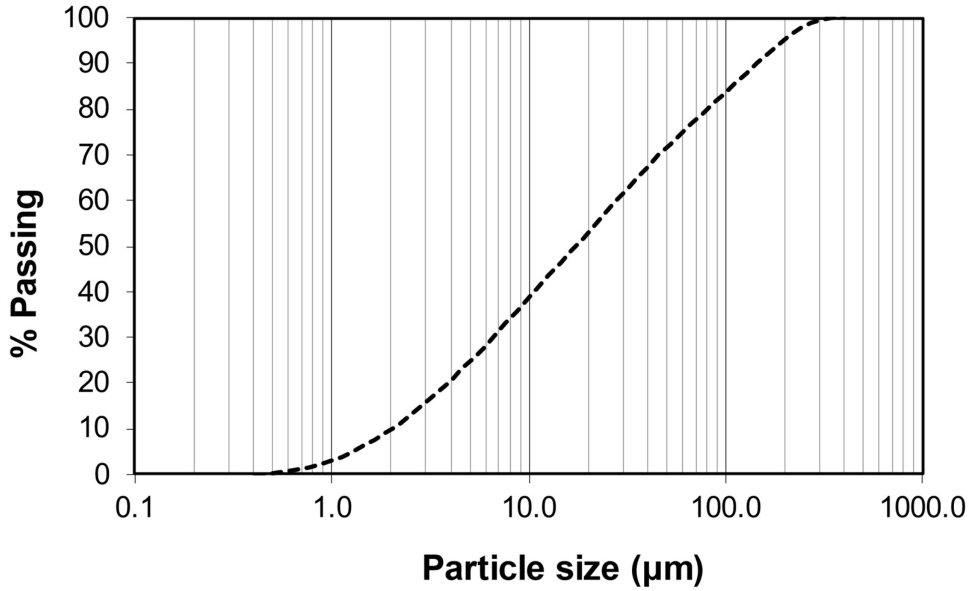

Fig. 3. Particle size distribution of the crushed sand obtained using laser diffraction ("% Passing" on the y-axis represents the percentage of particles in the sample that have a size smaller than or equal to a particular particle size on the x-axis)

554

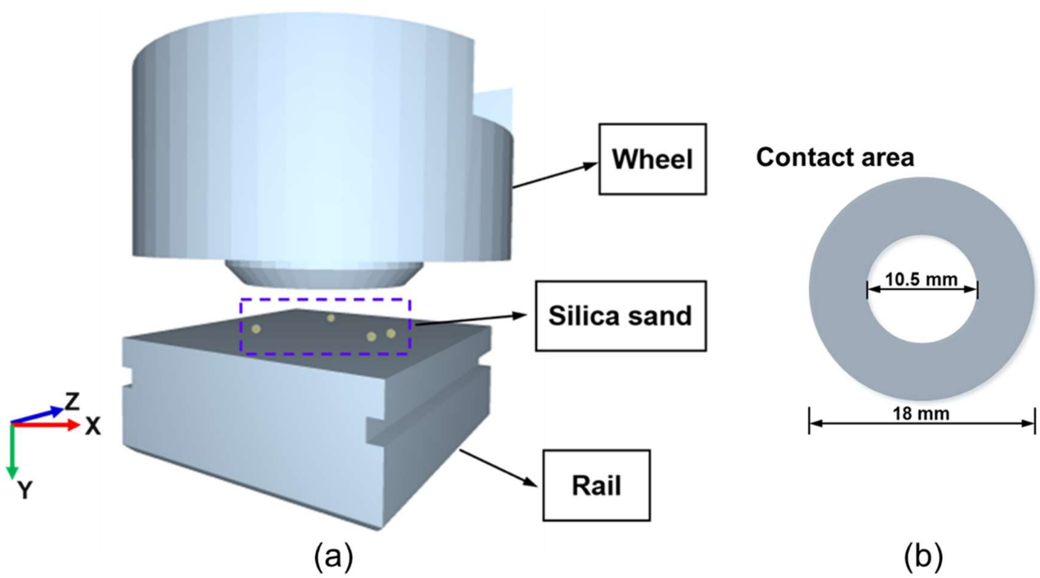

555

556 **Fig. 4.** (a) The set-up used for numerical modelling of the high-pressure torsion test and (b) the
557 dimensions of the annular contact area between the wheel and the rail specimens

558

559

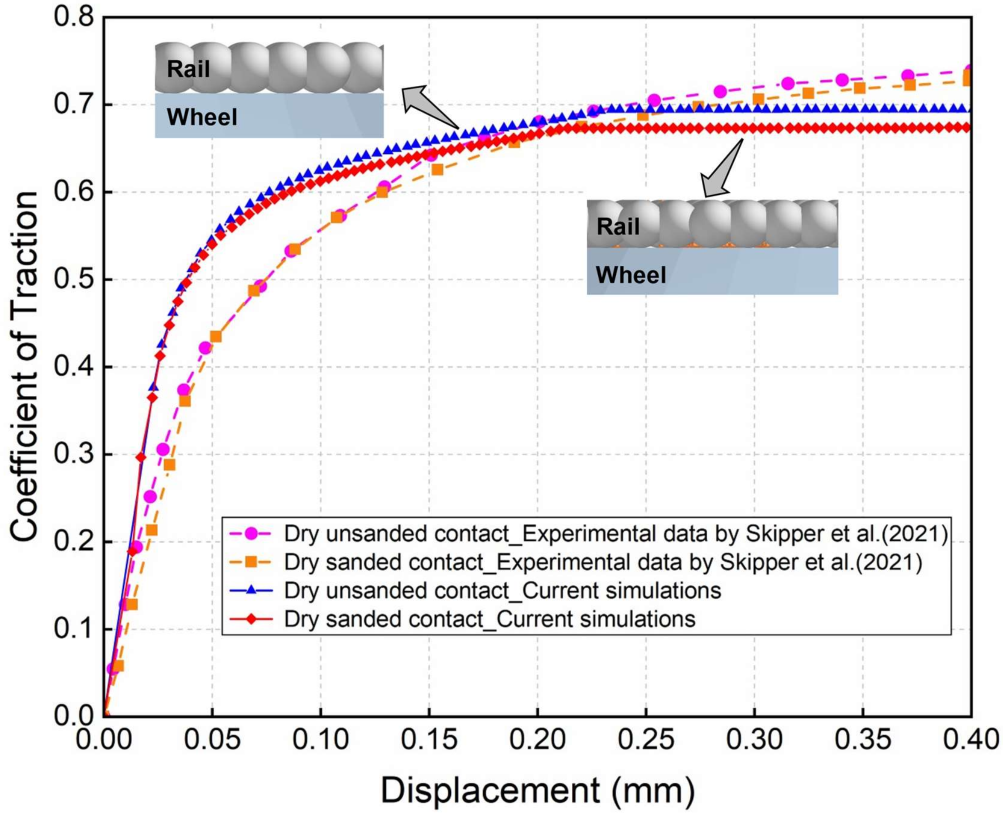

Fig. 5. Comparison of the coefficient of traction obtained from DEM modelling of the HPT set-up with and without the presence of sand particles under dry contact condition with the corresponding experimental data. (The light grey particles represent the rail specimen, and the orange particles represent the fragments of sand particles)

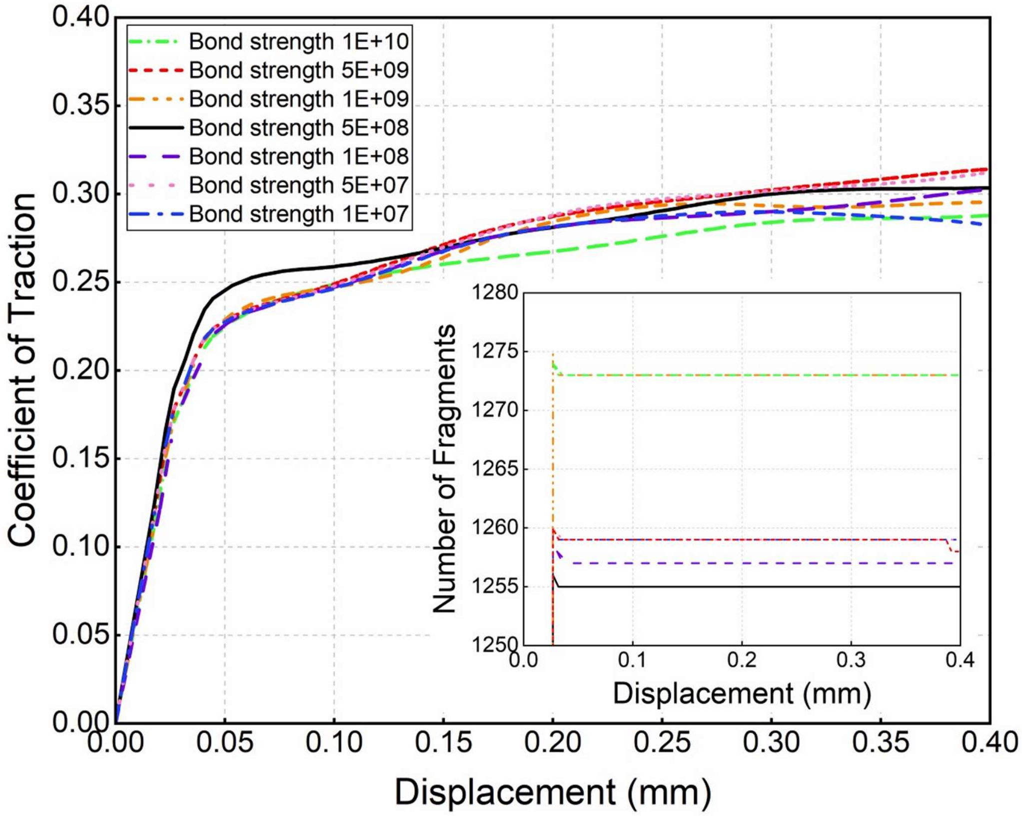

Fig. 6. Comparison of the coefficient of traction obtained from DEM modelling of the HPT set-up using different values of bond strength (The insert graph shows the number of fragments remaining on the contact area for each value of the bond strength)

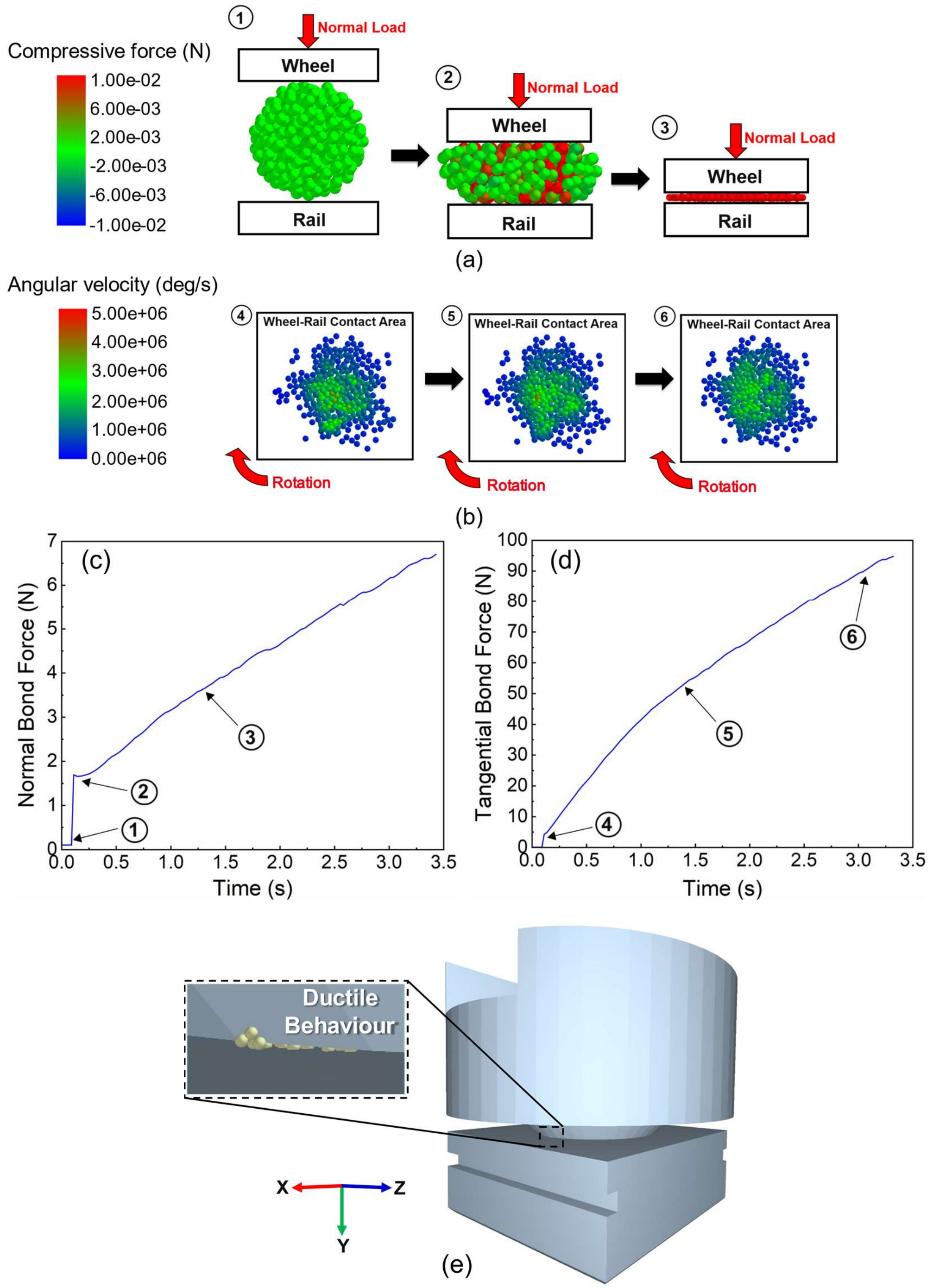

Fig. 7. The breaking behaviour of the sand particle and the evolution of the bond force in the normal and tangential directions for particle with a 1.0 mm diameter, and a bond strength and stiffness of 1.0e[10] [Pa] and 1.0e[10] [N/m^3], respectively, during the DEM modelling: (a) Changes in the compression force of fragments during compaction (side view), (b) Changes in the angular velocity of the fragments during torsion (top view), (c) Normal bond force, (d) Tangential bond force, and (e) the particle showing ductile behaviour when breaking

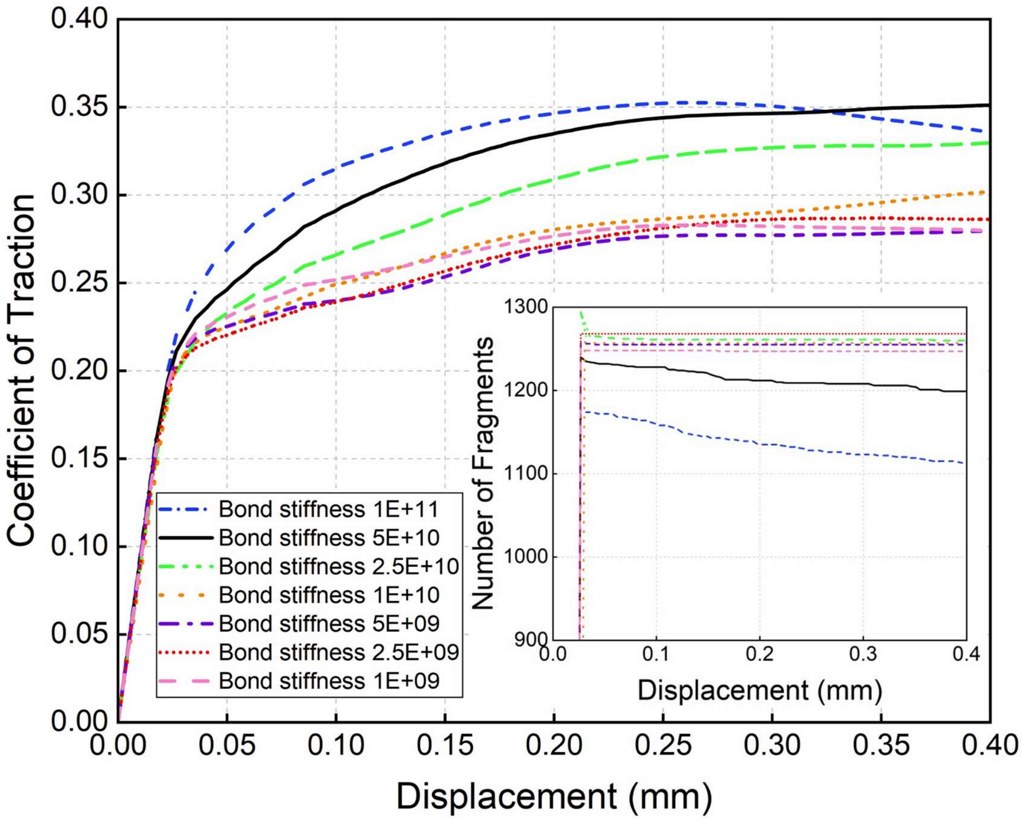

Fig. 8. Comparison of the coefficient of traction obtained from DEM modelling of the HPT set-up using different values of bond stiffness (The insert graph shows the number of fragments remaining on the contact area for each value of the bond stiffness)

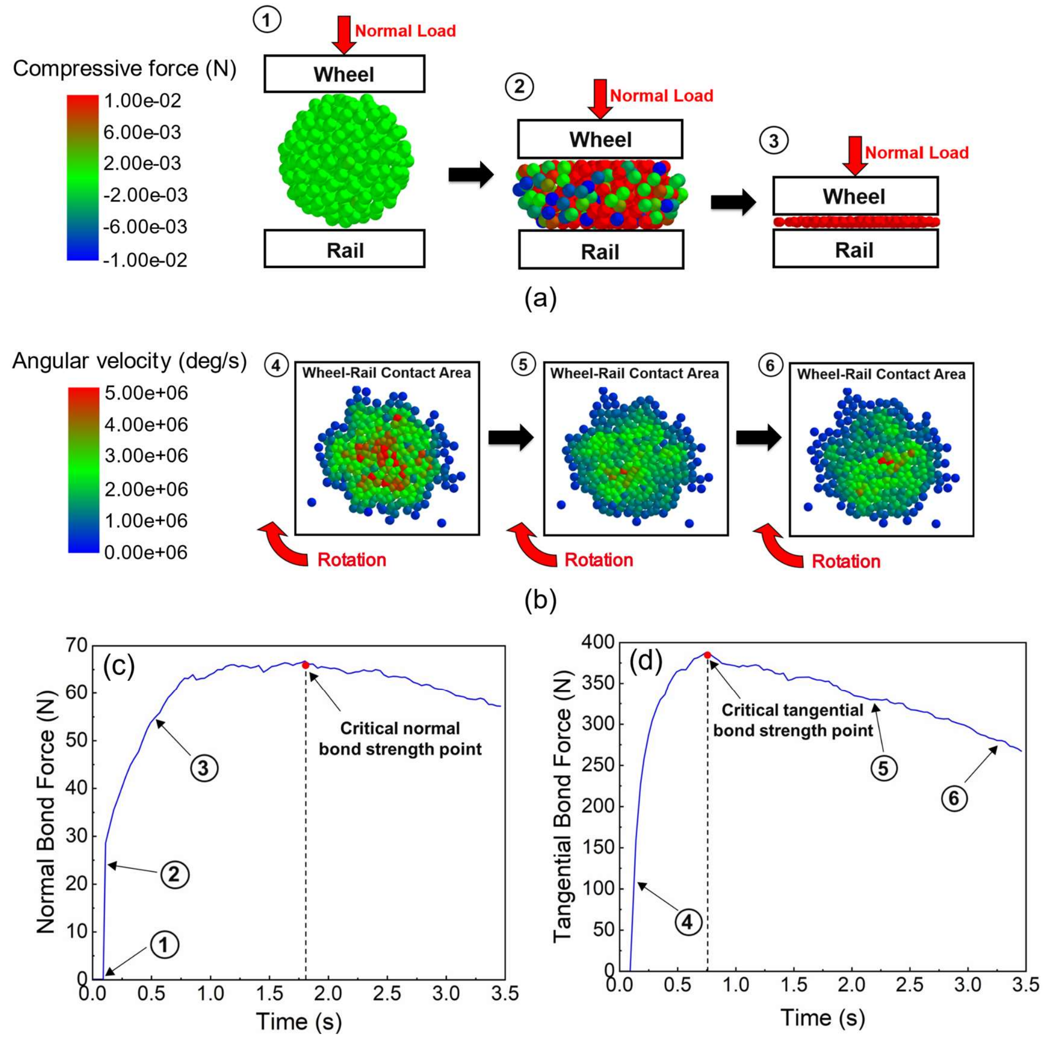

Fig. 9. The breaking behaviour of the sand particle and the evolution of the bond force in the normal and tangential directions for particle with a 1.0 mm diameter, and a bond strength and stiffness of 1.0e^{8} [Pa] and 1.0e^{11} [N/m^{3}], respectively during the DEM modelling: (a) Changes in the compression force of fragments during compaction (side view), (b) Changes in the angular velocity of the fragments during torsion (top view), (c) Normal bond force, and (d) Tangential bond force

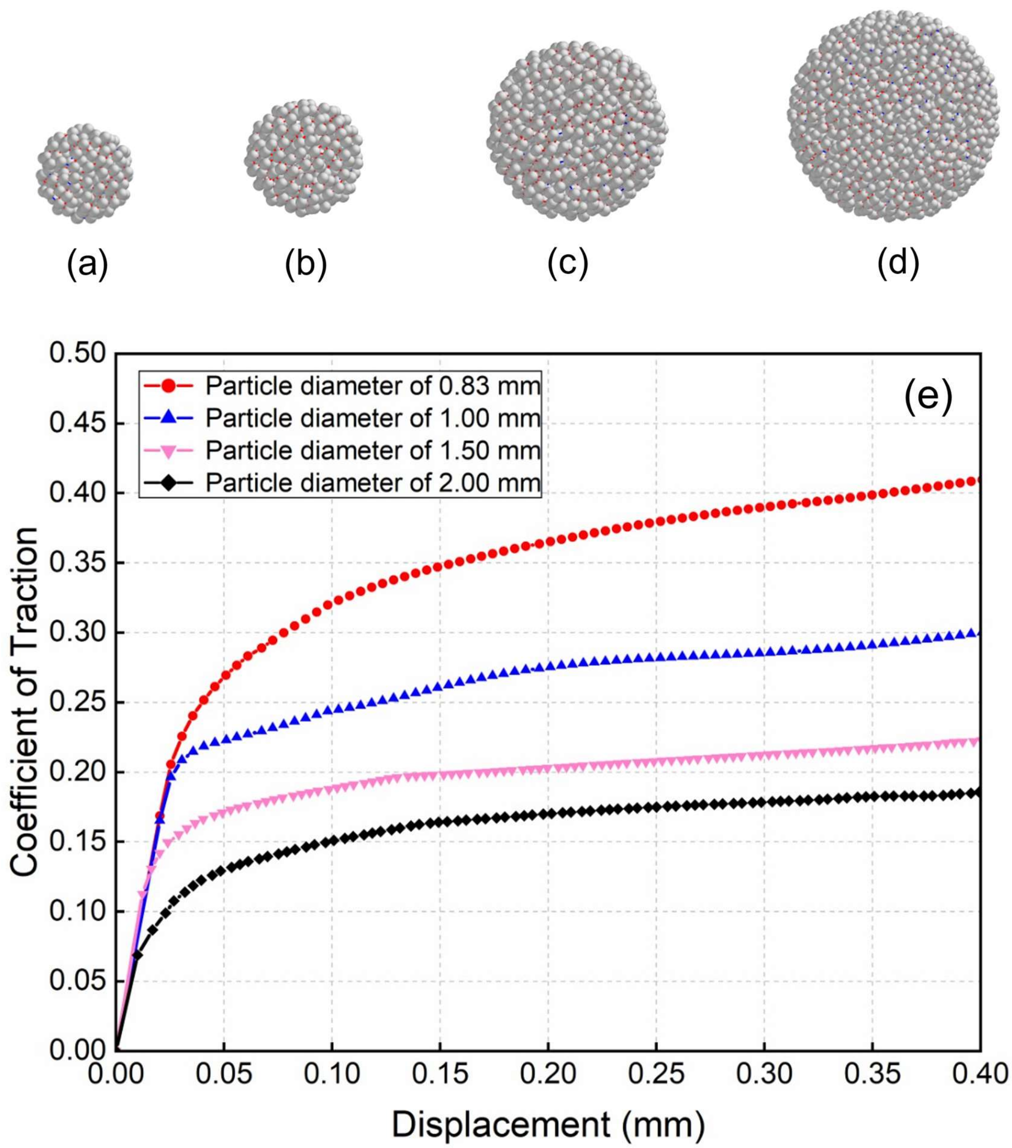

Fig. 10. Sand particles of different size with a diameter of: (a) 0.83mm, (b) 1.0mm, (c) 1.5mm, and (d) 2.0mm used in the DEM models and (e) comparison of the coefficient of traction obtained from DEM modelling of the HPT set-up using different particle sizes

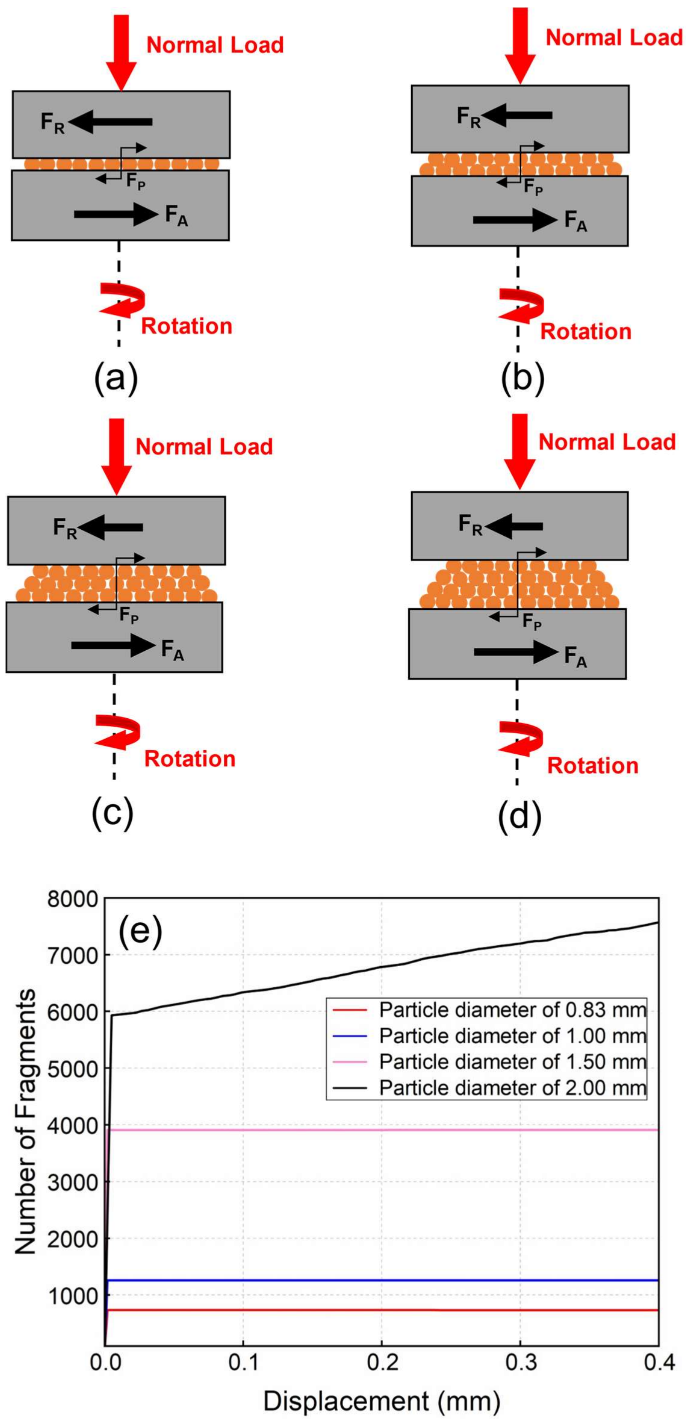

Fig. 11. Particle breakage in the contact area, the variation in the number of fragments depending on the particle size, and the possibility of the formation of fragment clusters and weak shear bands during the DEM simulation for particles with a diameter of: (a) 0.83mm, (b) 1.0mm, (c) 1.5mm, and (d) 2.0mm, and (e) comparison of the number of fragments produced during the DEM modelling of the HPT set-up for the above four particle sizes

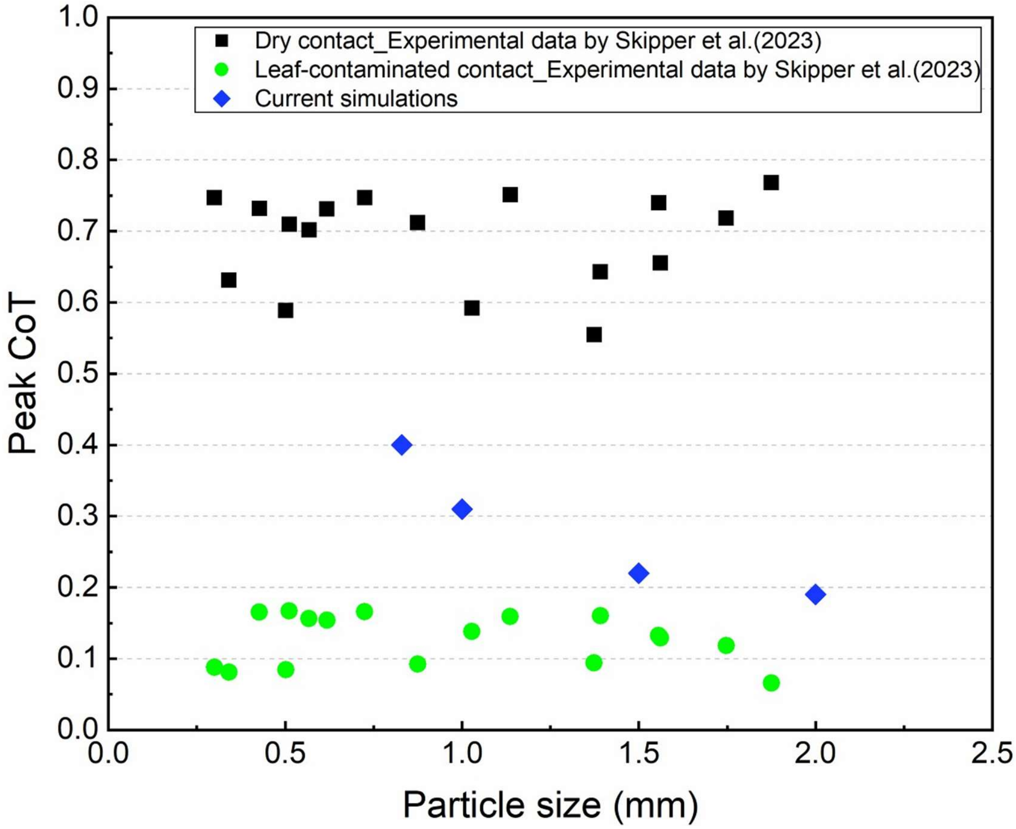

Fig. 12. Comparison of the peak coefficient of traction obtained from DEM modelling of the HPT set-up (blue diamond) using different particle sizes to the experimental results for dry (black square) and leaf-contaminated (green circle) contact condition by Skipper et al. (2023)

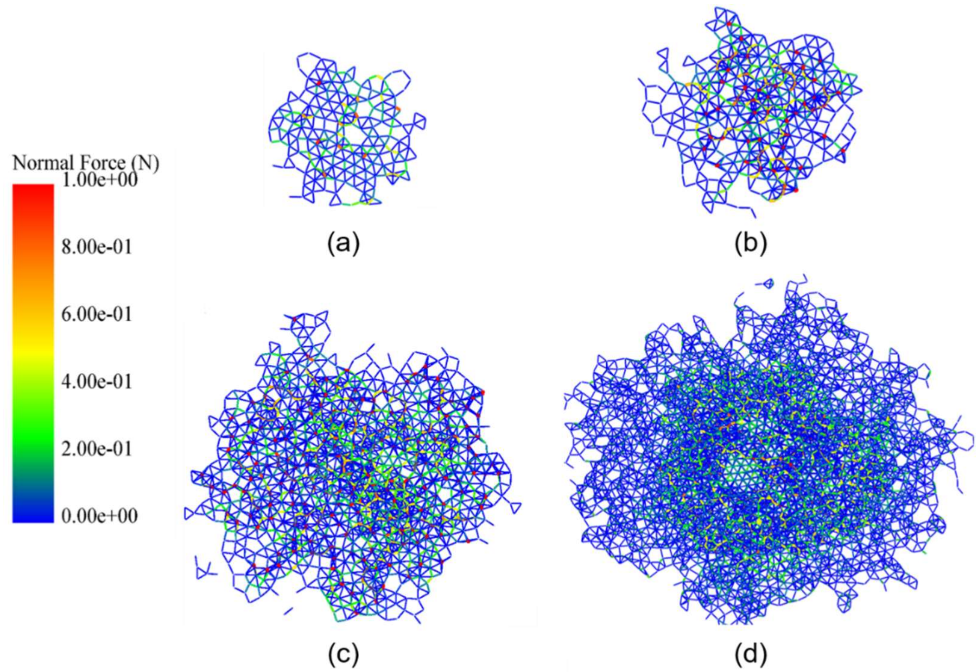

Fig. 13. The contact force network formed during crushing of a particle with a diameter of: (a) 0.83mm, (b) 1.0mm, (c) 1.5mm, and (d) 2.0mm obtained from the DEM models

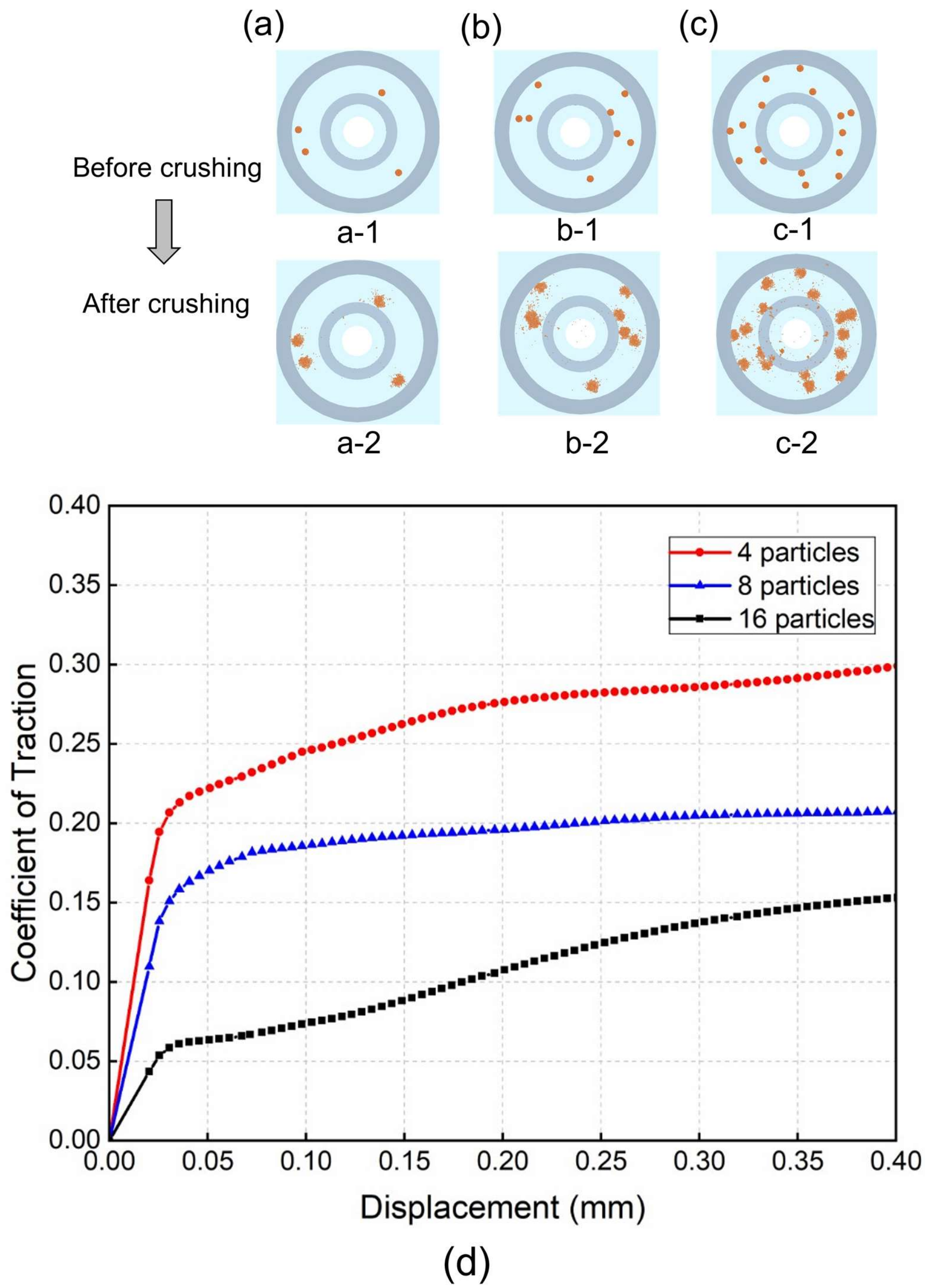

Fig. 14. The particle distribution used in the DEM models for different number of particles present at the wheel-rail contact area (1) before and (2) after crushing shown from the top view for: (a) 4 particles, (b) 8 particles, and (c) 16 particles and (d) comparison of the coefficient of traction obtained from DEM modelling of the HPT set-up using different number of particles at the contact area

Table 1 Material properties used as input parameters in the DEM modelling of the HPT set-up

Material	Parameters	Value
Silica Sand	Poisson's ratio (υ_m)	0.3
	Density (ρ), kg/m^3	2.65E+04
	Young's modulus (E), GPa	0.7
Wheel	Poisson's ratio (υ_m)	0.28
	Density (ρ), kg/m^3	7850
	Young's modulus (E), GPa	229.45
Rail	Poisson's ratio (υ_m)	0.3
	Density (ρ), kg/m^3	7850
	Young's modulus (E), GPa	210
Interaction	**Parameters**	**Value**
Particle to Particle	Coefficient of restitution (e_p)	0.8
	Coefficient of static friction (μ_s)	0.5
	Coefficient of rolling friction (μ_r)	0.01
Particle to Steel	Coefficient of restitution (e_p)	0.8
	Coefficient of static friction (μ_s)	0.5
	Coefficient of rolling friction (μ_r)	0.01

Table 2 Bond properties used as inputs in the BPM for the sand particles

Bond parameters	Value
Normal stiffness (k_n), N/m³	1.0E+10
Stiffness ratio $\left(k_n/k_t\right)$	1.0
Critical normal strength $(\sigma_{\max})$, Pa	1.0E+8
Strength ratio $\left(\sigma_{\max}/\tau_{\max}\right)$	1.0
Bonded disk scale (λ)	1.25

640

641 **Table 3** Particle properties used as input parameters in each numerical case study

Case No.	Bond strength [Pa]	Bond stiffness [N/m^3]	Particle diameter [mm]	Number of particles
Un-sanded	-	-	-	-
Sanded	1.0E+8	1.0E+10	0.83	4
a.1	1.0E+7	1.0E+10	1.0	4
a.2	5.0E+7	1.0E+10	1.0	4
a.3	1.0E+8	1.0E+10	1.0	4
a.4	5.0E+8	1.0E+10	1.0	4
a.5	1.0E+9	1.0E+10	1.0	4
a.6	5.0E+9	1.0E+10	1.0	4
a.7	1.0E+10	1.0E+10	1.0	4
b.1	1.0E+8	1.0E+9	1.0	4
b.2	1.0E+8	2.5E+9	1.0	4
b.3	1.0E+8	5.0E+9	1.0	4
b.4	1.0E+8	1.0E+10	1.0	4
b.5	1.0E+8	2.5E+10	1.0	4
b.6	1.0E+8	5.0E+10	1.0	4
b.7	1.0E+8	1.0E+11	1.0	4
c.1	1.0E+8	1.0E+10	0.83	4
c.2	1.0E+8	1.0E+10	1.0	4
c.3	1.0E+8	1.0E+10	1.5	4
c.4	1.0E+8	1.0E+10	2.0	4
d.1	1.0E+8	1.0E+10	1.0	4
d.2	1.0E+8	1.0E+10	1.0	8
d.3	1.0E+8	1.0E+10	1.0	16

642

643

Table 4 Fragment and bond properties as well as the average effective radius for each particle size

Particle diameter [mm]	Number of fragments	Number of bonds	Fragments diameter [mm]	Average effective radius of friction in HPT [mm]
0.83	210	486	0.1	7.52
1.0	326	739	0.1	7.40
1.5	1000	2892	0.1	7.24
2.0	2840	6855	0.1	7.32

Table 5 Fragment properties and the average effective radius for the three different number of particles present on the contact area

Number of particles	Number of Fragments	Fragments diameter [mm]	Average effective radius of friction in HPT [mm]
4	1304	0.1	7.40
8	2608	0.1	7.11
16	5216	0.1	7.08